
Single mRNP analysis by super-resolution microscopy and fluorescence correlation spectroscopy reveals that small mRNP granules represent mRNA singletons

Àngels Mateu-Regué¹, Jan Christiansen², Frederik Otzen Bagger¹,
Christian Hellriegel³ and Finn Cilius Nielsen^{*1}

¹*Center for Genomic Medicine, Rigshospitalet,*

²*Department of Biology, University of Copenhagen, Denmark and*

³*Carl Zeiss Microscopy GmbH, Jena, Germany*

¹ Center for Genomic Medicine, Rigshospitalet, 2100 Copenhagen, Denmark

² Department of Biology, Copenhagen Biocenter, 2200 Copenhagen, Denmark

³ Carl Zeiss Microscopy GmbH, 07745 Jena, Germany

*Correspondence: finn.cilius.nielsen@regionh.dk

Abstract

Small cytoplasmic mRNP granules are implicated in mRNA transport, translational control and decay. Employing Super-resolution Microscopy and Fluorescence Correlation Spectroscopy, we analyzed the molecular composition and dynamics of single cytoplasmic YBX1_IMP1 mRNP granules in live cells. Granules appeared elongated and branched with patches of IMP1 and YBX1 distributed along mRNA, reflecting the attachment of the two RNA-binding proteins in *cis*. Particles form at the nuclear pore and are spatially segregated from translating ribosomes, so the mRNP is a repository for mRNAs awaiting translation. Individual mRNPs contain a single mRNA and 5 to 15 molecules of YBX1 and IMP1, which is in agreement with the average number of mRNA-binding sites calculated from CLIP analyses. We conclude that small cytoplasmic mRNP granules are mRNA singletons, thus depicting the cellular transcriptome. Consequently, expression of functionally related mRNAs in RNA regulons is unlikely to result from coordinated assembly.

Keywords: RNA granules, mRNP granules, IMP1, YBX1, Singleton, Structured Illumination Microscopy, Localization Microscopy, Fluorescence Correlation Spectroscopy, mRNA regulons

Introduction

Essential steps from the nuclear mRNA processing and export to cytoplasmic localization, translation and decay of mRNAs are implicated in fine tuning of gene expression. Regulatory steps are governed by RNA-binding proteins, which interact with the mRNA in a sequential manner. Mammalian cells comprise about 1500 RNA-binding proteins of which nearly half bind to mRNAs (Gerstberger et al., 2014), and the majority is widely distributed with a minority exhibiting a particular spatial and temporal expression. Some mRNA-binding proteins shuttle between the nucleus and the cytoplasm, whereas others are mainly present in the cytoplasm (Shyu and Wilkinson, 2000), including proteins such as FMRP, HuD as well as YBX1 and the family of insulin-like growth factor 2 mRNA binding proteins IMP1, 2 and 3 (Darnell and Richter, 2012). Cytoplasmic mRNA-binding proteins are found in small membrane-less granules. In contrast to the larger P-bodies and stress granules, which mostly embody stress-induced condensations of RBPs and mRNA promoted via intrinsic disordered regions in the attached RBPs (Molliex et al., 2015; Reijns et al., 2008), small cytoplasmic mRNP granules represent the unperturbed state of cellular mRNA. Due to their significance in dendritic and axonal mRNA transport, cytoplasmic mRNP granules are sometimes referred to as neuronal RNP granules (Anderson and Kedersha, 2006; Kiebler and Bassell, 2006), but mRNP granules are found in any cell throughout the body at all developmental stages. Global biochemical analyses have shown that granules contain ribosomal subunits, translation factors, decay enzymes, helicases, scaffold proteins, and RNA-binding proteins, but we have limited data about the molecular composition of individual granules, that allow us to understand their function and relation to the other granular assemblies.

Insulin-like growth factor 2 (IGF2) mRNA-binding protein 1 (IMP1, IGF2BP1) belongs to a conserved family of heterochronic mRNA-binding proteins (IMP1, IMP2, and IMP3) (Hansen et al., 2004; Nielsen et al., 2001; Nielsen et al., 1999; Yaniv and Yisraeli, 2002). Together with the cytoplasmic mRNA-binding protein YBX1, IMPs form typical cytoplasmic RNP granules (Eliscovich et al., 2017) (Figure 1). Granules are mobile and widespread in the cytoplasm although they exhibit a preponderance for the perinuclear regions and the

lamellipodia in motile cells (Nielsen et al., 1999; Oleynikov and Singer, 2003). In conventional laser scanning microscopy they exhibit an optical diameter of about 200-700 nm (Nielsen et al., 2002). Transcriptome-wide CLIP analyses have shown that both IMP1 and YBX1 associate with large parts of the transcriptome (Conway et al., 2016; Goodarzi et al., 2015). Individual RNAs exhibit numerous IMP1 and YBX1 attachment sites distributed along the target mRNA (Nielsen et al., 2004; Runge et al., 2000; Singh et al., 2015), although it is unknown whether binding is taking place on the same mRNA molecule. IMP1 and YBX1 are essential for normal development; IMP1- and YBX1-deficient mice are both small with imperfect organ development including neuronal defects (Hansen et al., 2004; Uchiumi et al., 2006), and at the cellular level both factors promote cell growth (Bell et al., 2013; Bommert et al., 2013; Shiota et al., 2008). Moreover, YBX1 and IMP1 have been implicated in a series of complex biological pathways such as F-actin formation and protein secretion (Jønsen et al., 2007; Uchiumi et al., 2006), and specifically IMP1 is a participant in the embryonal heterochronic network consisting of *HMGA2*, *let-7* and *Lin28B* mRNAs (Jonson et al., 2014; Nishino et al., 2013). Finally, YBX1 plays a role in nodal signaling via *sqt* RNA localization, processing and translation (Kumari et al., 2013).

To advance our understanding of cytoplasmic mRNP granules, we employed super-resolution and fluorescence correlation microscopy of YBX1, IMP1 and associated mRNA. In contrast to the current perception based on conventional light microscopy, our data show that granules represent irregular branched and elongated structures composed of alternating patches of IMP1 and YBX1 along a common mRNA. Formation of the particles requires mRNA, and mRNPs are first observed at the nuclear pore. The mRNPs are not connected to actively translating ribosomes, which are located in a separate vicinal compartment. Each particle contains a single mRNA and between 5-15 IMP1 and YBX1 molecules, in agreement with the average number of binding sites in the target mRNAs. Taken as a whole, we conclude that mRNP granules represent singletons and that coordinated expression of functionally related mRNAs is unlikely to be due to coordinated assembly.

Results

IMP1 and YBX1 coexist in mRNPs in an RNA-dependent manner

To provide an overview of the subcellular distribution and structure of IMP1 and YBX1 RNPs *in vivo*, HeLa cells were stained with anti-IMP1 and anti-YBX1 antibodies and examined by Structured Illumination Microscopy (SIM). IMP1 and YBX1 were cytoplasmic and prominent at the perinuclear region and in the lamellipodia of the cells (Figure 2A-C). Granules appeared branched and elongated and ranged from 250 to 800 nm in size and were composed of alternating patches of IMP1 and YBX1 (Figure 2D-F). In general, YBX1 was observed along the entire outline of the particle, whereas IMP1 exhibited a preponderance for projections and ends. To visualize the associated mRNA, we performed FISH of *ACTB* mRNA combined with immunostaining of YBX1 and IMP1 (Figure 2N-R). *ACTB* mRNA was hybridized to 48 labelled Quasar® 570 Dye-labeled probes covering the entire mRNA from the 5' to the 3' end. Probe staining was partially masked by the attached RNA-binding proteins, in particular when YBX1 was present. To corroborate the putative RNA-dependent interaction of YBX1 and IMP1, an immunoprecipitation of 3xFLAG-tagged or GFP-tagged IMP1 was carried out (Supplemental Figure 1). YBX1 was enriched in the immunoprecipitate, and treatment with RNase A reduced the amount of immunoprecipitated YBX1, indicating that IMP1 does not interact directly with YBX1. In agreement with the observation that the particles contain multiple IMP1 molecules binding independently to the mRNA, IMP1 was also reduced by RNase A (Supplemental Figure 1B). The mRNPs were clearly distinct from cytoplasmic P-bodies and stress-granules identified by G3BP and DCP1a, respectively (Figure 2G-H and Supplemental Figure 2). The average size of stress-granules were at least an order of magnitude larger than IMP1_YBX1 mRNPs, that could be distinguished within the larger bodies.

YBX1 and IMP1 mRNP is formed in the nuclear pore and awaits translation

Since the observed size of the mRNP is difficult to reconcile with facilitated diffusion of IMP1_YBX1 mRNP particles through the central nuclear pore channel, whose size limit is regarded to be about 40 nm (Hoelz et al., 2011), we examined the first appearance of the mRNP. SIM revealed very faint and almost non-existent

YBX1 and IMP1 nuclear staining, and we failed to observe any colocalization between the two factors and mRNA. This led us to image the nuclear pore in closer detail. Nuclear pores were visualized by staining of Nup153, and both IMP1 and YBX1 mRNPs were found to align with the pore (Figure 3), where mRNPs projected towards the cytoplasm. The cytoplasmic distribution and alignment was unaffected by incubation with leptomycin (data not shown). We infer that IMP1_YBX1 mRNPs are likely to form at the nuclear pore. To define the relation of the mRNP to the translation apparatus, we employed O-propargyl-puromycin (OPP) to depict actively translating ribosomes (Liu et al., 2012). After fixation, OPP was conjugated to an Alexa Fluor-488 fluorophore by click chemistry. Moreover, IMP1 and YBX1 were stained by immunofluorescence, and SIM Z-stacks of the cells were generated. As shown in Figure 4 (Panels A and B) and supplemental Figure 3, IMP_YBX1 mRNP did not colocalize with translating ribosomes. However, ribosomes were positioned in close proximity to the mRNPs, facilitating a possible handover of mRNA. To substantiate the cytological findings, we performed a polysome fractionation analysis confirming that both IMP1 and YBX1 predominantly sedimented as free mRNP in monosomal fractions corresponding to 40S - 80S (Figure 4C). Moreover, we performed an immunofluorescence staining combining IMP1 and the elongation factor eEF1A or eIF4A3. In its GTP-form, eEF1A is responsible for bringing aminoacyl-tRNA to the A-site of the ribosome, whereas eIF4A3 is a core component in the exon junction complex defining virgin mRNAs (Maquat et al., 2010; Mateyak and Kinzy, 2010) (Figure 4, panel D). eEF1A was absent from mRNPs, whereas eIF4A3 colocalized with the mRNP. The results are in agreement with a spatial segregation of mRNPs from actively translating ribosomes and imply that protein synthesis follows unloading of the mRNA.

Dynamics of IMP1_YBX1 mRNPs

To assess the dynamics of cytoplasmic IMP1_YBX1 mRNPs, we employed Fluorescence Correlation Spectroscopy (FCS). Wild-type GFP-tagged IMP1 and -YBX1 and a GFP-tagged IMP1 GXXG mutant (GFP-IMP1_KH1-4mut), with impaired RNA-binding (Supplemental Figure 4), were expressed in HeLa cells. Moreover, GFP was included as a reference. As depicted in Figure 5A, GFP and GFP-IMP1_KH1-4mut exhibited faster Lag times than GFP-IMP1 and GFP-YBX1. Whereas GFP best fitted a 1-component model, the best fit of the experimental autocorrelation curves of GFP-IMP1_KH1-4mut, GFP-IMP1 and GFP-YBX1 was a

2-component model. The modelling showed that GFP-IMP1_KH1-4mut could be resolved into two relatively fast diffusion times of 2.9E-04 s and 1.2E-03 s, respectively, whereas GFP-IMP1 and GFP-YBX1 exhibited a fast moving fraction with a Lag time of $\sim 10\text{E-}03$ s and a much slower fraction moving in the range of $10\text{E-}01$ s (Figure 5C). Compared to GFP, wild-type IMP1 and YBX1 exhibited fractions diffusing 10 fold and a 1000 fold slower. In agreement with the pull-down analysis described above, Fluorescence Cross Correlation Spectroscopy with GFP-IMP1 or GFP-IMP1_KH1-4mut combined with mCherry-YBX1 demonstrated that the interaction between the two factors *in vivo* relies on mRNA-binding and not on other factors (Figure 5B). To further substantiate FCS data, we visualized the mobility of the RNP in the live cell. We employed mEos3.2, a photoconvertible fluorescent protein (Zhang et al., 2012), and expressed mEos3.2-IMP1. After localized photoactivation at 405 nm, cellular movements of the photoconverted red mEos3.2-IMP1 was followed by time lapse microscopy (Supplementary Figure 5). Both a slow and a rapid transport (in the range of seconds) was observed. Slow particles diffused in all directions and migrated at very slow rate of about $0.1\text{ }\mu\text{m/s}$. Even after 1.5 minute the majority of the granular RNP remained in the center of the photoactivation. In contrast, the rapid diffusion accumulated quickly at a particular distant site $25\text{ }\mu\text{m}$ away within seconds after photoconversion, corresponding to a speed of at least $\sim 5\text{ }\mu\text{m/s}$. The results show that assembly of granules requires RNA-binding, and that IMP1_YBX1 mRNP motility is multidirectional and involves fast and slow trafficking and regulated anchoring.

Molecular composition of IMP1_YBX1 mRNP

We analysed the number of molecules in IMP1_YBX1 mRNP *in vivo* by means of Fluorescence Correlation Spectroscopy (FCS) and Localization Microscopy and compared the results to available transcriptome-wide IMP1 and YBX1 eCLIP and RIP-seq data. Moreover, the interplay between IMP1 and YBX1 upon binding to high-affinity RNA targets such as *ACTB* and *C-MYC* mRNAs (Leeds et al., 1997; Ross et al., 1997), was examined in order to provide a framework for an understanding of the stoichiometric data (Figure 6).

Figure 6A shows a schematic representation of *ACTB* and *C-MYC* transcripts together with the CLIP-derived number of cross-linked and immunoprecipitated reads at particular positions (Conway et al., 2016; Goodarzi

et al., 2015). Although IMP1 exhibits a preponderance for the 3'UTR and YBX1 binding is more widespread, some binding sites are overlapping and the two factors may compete for a number of binding sites. The CLIP data show that YBX1 and IMP1 exhibit strong binding to *ACTB* mRNA exon 5 and the ZIP code in the 3'UTR, respectively, and to the CRD region and the 3'UTR of *C-MYC*, respectively. Therefore, we performed electrophoretic mobility-shift assays (EMSA) with these mRNAs, shown in Figure 6B. YBX1 and IMP1 concentration ratios were according to the protein copy number per HeLa cell, as previously characterised (Singh et al., 2015). YBX1, IMP1 or both proteins were incubated with the radioactively labelled RNA targets. The mobility-shifts showed that the binding of each protein to the chosen mRNA segments was mutually exclusive since there was no evidence of a supershift with any of the RNA probes. For *C-MYC*, we observed that both YBX1 and IMP1 were able to bind to the CRD and 3'UTR targets. IMP1 exhibited a higher affinity for CRD than YBX1, since at 1:10 of the YBX1 concentration IMP1 was able to out-compete YBX1. The same happened with *C-MYC* 3'UTR, although in this case IMP1 was able to achieve a higher degree of multimerization. Regarding the *ACTB* segments, we observed that YBX1 had a very high affinity for exon 5 and showed a high degree of multimerization, in accordance with the CLIP data. IMP1 was essentially unable to bind to *ACTB* exon 5 and could not compete with YBX1. Both IMP1 and YBX1 were able to bind to the 3'UTR target, and we observed the same competition pattern as described for the *C-MYC* transcripts, although both proteins exhibited lower affinity. Taken together, we infer that IMP1 and YBX1 compete for shared binding segments – so at a given time IMP1 or YBX1 may not occupy all their possible binding sites.

To determine the number of IMP1, YBX1 and RNA molecules in the individual mRNP, we employed Localization Microscopy and Fluorescence Correlation Spectroscopy. For Localization Microscopy, HeLa cells were stained with anti-IMP1 or anti-YBX1 antibodies and Alexa Fluor 568 or 555 secondary antibodies, respectively, or with a set of *ACTB* mRNA probes as shown in Figure 2. The number of secondary antibodies binding a primary antibody was determined by FCS, and this showed that two secondary antibodies bind to each primary antibody (data not shown). Consequently, events (emitted photons at a particular site) were divided by two (Figure 7C). To avoid counting the same secondary antibody more than once due to the presence of multiple fluorophores and to improve positioning accuracy, a grouping of 5.5 pixels was applied.

Panel A shows Localization Microscopy readings with GAUSS distributions and crosses. Clustered photons (crosses) corresponding to 50 granules were counted (Figure 7A), and the median and range are summarized in the Table (Figure 7C). The median number of molecules was 7 for YBX1 (range 2-34) and 6 for IMP1 (range 2-15) in the RNP. Moreover, we analyzed the number of *ACTB* RNA probes in the mRNP granules. As illustrated in Figure 2, parts of the *ACTB* mRNA appeared to be masked by attached RBPs, and we counted on average 11 probes ranging from 3-42 in the mRNP. In no *ACTB* cluster, we counted more than the maximal number of 48 probes. Therefore, we infer that there is only a single *ACTB* transcript in a particle.

To corroborate the findings described above, we extracted information regarding the average number of molecules in the particles in *live* cells by FCS. The counts per particle (related to the amplitude of the fluorescence fluctuations) of FCS measurements in the free GFP and GFP-IMP1_KH1-4mut constructs (monomers) were compared with the wild type GFP-IMP1 and GFP-YBX1 in HeLa cells. We could measure differences in the fluctuations during the recorded measurements (Figure 7B), and this was also represented in the amplitude of the autocorrelation curves. Cytoplasmic readings from 9 different cells showed that the number of GFP-IMP1 molecules per particle was from 7 to 11, considering GFP-IMP1_KH1-4mut as the monomer state of the protein, whereas the results for GFP-YBX1 were unexpectedly low compared to what we observed in the Localization Microscopy analysis. Endogenous YBX1 concentration is 10 times higher than IMP1, and we suspected that GFP-YBX1 counts per particle were underestimated due to the high levels of competing endogenous protein. To examine if this was the case, endogenous YBX1 was knocked down using a siRNA against the 3'UTR. As observed in Figure 7, counts per particle during these conditions increased from 3-4 to 8-13 YBX1 molecules per particle. Finally, we estimated the number of global IMP1 and YBX1 mRNA binding sites from public CLIP and RIP-seq data (Conway et al., 2016; Goodarzi et al., 2015) in order to put the Localization Microscopy and FCS data in perspective (Figure 7, Panel C). Raw CLIP-seq data (fastq) were downloaded from the short read archive (SRA) and aligned to the human genome sequence. Binding sites were estimated by read-islands. The lower detection level was adjusted to the nearest threshold, where islands in the mock control samples equalled the total number of transcripts, therefore a cut-off of 7 and 6 for IMP1 and YBX1, respectively, was employed. We estimated that the average number of IMP1 and YBX1

binding sites per mRNA to be 7 and 5, respectively. IMP1 has been described to dimerize to form stable RNA-binding complexes (Nielsen et al., 2004), corroborated by the electrophoretic mobility-shift analysis in Figure 6, and YBX1 has also been shown to multimerize on a single RNA attachment site (Figure 6) (Skabkin et al., 2004). Taken as a whole, Localization Microscopy and FCS analyses, which provide the molecular composition of the individual RNP granules *in vivo*, are in agreement with the transcriptome-wide CLIP estimates, when dimerization of IMP1 and a multimerization of YBX1 on mRNA are taken into account. We therefore conclude that IMP1_YBX1 RNPs represent solitary mRNAs with attached proteins.

Discussion

Cytoplasmic RNP granules have been recognized for several decades, and although we have a relatively deep understanding of their biochemistry, the molecular composition and cellular distribution are incompletely understood. This has partly been due to the lack of technologies to characterize molecular complexes in intact and live cells, so we employed super resolution microscopy and correlation spectroscopy to provide a deeper insight into the nature of single mRNP granules.

Compared to conventional laser scanning microscopy, where mRNP granules appear spherical with a size of 200-700 nm (Nielsen et al., 2002), structured illumination microscopy (SIM) has a resolution 2-3 times below that of diffraction-limited instruments, providing a lateral resolution of about 100 nm (Stelzer, 2014). An average 2 kb mRNA has an outline of about 300 nm - taking secondary structure into account - so it is feasible to distinguish RBPs on the same mRNA by SIM (Milo et al., 2010) (<http://book.bionumbers.org/which-is-bigger-mrna-or-the-protein-it-codes-for/>). IMP1_YBX1 mRNPs were on average 300 nm in size, which is in agreement with atomic force microscopy of isolated granules (Jønson et al., 2007). YBX1- and IMP1-stainings were partly overlapping but also alternating along the mRNP. Whereas YBX1 was distributed along the entire particle, IMP1 had a preponderance for projections and ends. YBX1 is one of the core proteins of mRNPs and has previously been described to coat the entire mRNA (Singh et al., 2015; Skabkin et al., 2004), whereas IMP1 preferentially binds to single-stranded CA-rich elements in the 3'UTR and loop regions (Conway et al., 2016; Hafner et al., 2010). As previously described, the embedded mRNAs were to a large extent masked by the associated proteins (Buxbaum et al., 2014). In our data, mRNA appeared to be masked particularly in regions covered by YBX1, which is in accordance with the fact that YBX1 acts as a translational repressor (Evdokimova et al., 2006). Due to the distinct localization of the core proteins in the mRNP, the complete structure was only perceived in the composite pictures. If focus had been directed towards one of the factors, we would have failed to recognize the entire size and shape of the mRNP. Moreover, SIM directly demonstrates that YBX1 and IMP1 bind in *cis*, which is of significance for the interpretation of CLIP and immunoprecipitation analysis that fail to make a distinction between *cis* and *trans*.

RNA-binding proteins associate with and dissociate from the mRNA along its journey from the nucleus to the translating ribosomes (Singh et al., 2015). Based on the presence of nuclear export signals in IMP1 and YBX1, the general idea has been that the factors enter the nucleus and bind their target mRNAs (Nielsen et al., 2003; Oleynikov and Singer, 2003). We hardly observed nuclear IMP1 and YBX1 staining, and proper mRNP complexes composed of IMP1 and YBX1 and mRNA were only identified at the cytoplasmic side of the nuclear pore. This observation supports a recent study, indicating that *Actb* mRNA first associates with IMP1 in the nuclear envelope (Wu et al., 2015). The nuclear pore is flexible and dynamic (Knockenbauer and Schwartz, 2016), and the largest macromolecular complexes that have been shown to pass are viral capsids up to ~40 nm diameter. Our data reflect that the mRNA is brought to the pore by a canonical mRNA export pathway, before IMP1 and YBX1 are loaded onto the mRNA. In this way, the nuclear pore may represent a crucial remodeling step of the mRNP (Singh et al., 2015). Whether the nuclear export signals in IMP1 and YBX1 have a function in localization to the nuclear pore remains to be addressed.

In the cytoplasm, IMP1 and YBX1 protect mRNAs from miRNA-mediated degradation (Jonson et al., 2014) and YBX1 is also a mRNA stabilizer (Evdokimova et al., 2001), so the mRNP is considered an mRNA repository/safe house until translation. Although granules incorporate ribosomal subunits (Krichevsky and Kosik, 2001), we observed no direct association with translating ribosomes, which were closely intertwined between the mRNPs. The mRNP also contained the exon-junction complex core factor eIF4A3, which is a hallmark of mature mRNA prior to the pioneer round of translation. Our earlier compositional analysis of IMP1 RNPs, that identified the remaining exon-junction components together with the nuclear cap-binding subunit CBP80 and the nuclear poly(A)-binding protein PABPN1, corroborates the pre-translational status of these cytoplasmic mRNPs (Jønson et al., 2007). In agreement with their large composite nature the majority of the mRNPs exhibited a very slow diffusion rate compared to the KH domain GXXG loop mutant that failed to bind RNA. Particles migrated in all directions, and judged from the photoconversion experiments some were almost immobile, whereas about one-third of the mRNPs exhibited a faster mobility. The fastest particles were able to migrate several micrometers per second. Intriguingly, they accumulated at a particular location indicating that they may be subject to a regulated cytoplasmic docking. Transport may involve simple diffusion but also cytoplasmic streaming and motors, which are not mutually exclusive mechanisms (Lu et al.,

2016; Song et al., 2015; Suzuki et al., 2017). Moreover, the single photoconverted mRNP was fairly stable, indicating that fluidity is low in contrast to what is observed within liquid droplets (Courchaine et al., 2016).

We determined the molecular composition of the individual granules by Localization Microscopy and FCS. Both methods roughly led to the same result and showed that particles were composed of 5-15 molecules of both IMP1 and YBX1. Due to the masking, the Localization Microscopy analysis of *ACTB* mRNA should obviously be interpreted with some caution. However, since we never arrived at probe counts exceeding the total number of applied *ACTB* probes, we infer that there is only one *ACTB* mRNA in the particles in agreement with what we observed by SIM. Moreover, the comparative data from CLIP analysis (Conway et al., 2016; Goodarzi et al., 2015) show - in agreement with the Localization Microscopy and FCS data - that the average number of YBX1 and IMP1 mRNA attachment sites at a global level are 6 and 7, respectively. The reason that FCS and Localization Microscopy provide slightly higher numbers of IMP1 molecules is in agreement with IMPs binding as dimers and that YBX1 to some extent multimerizes. The results are in line with recent findings showing that neuronal mRNAs travel singly into dendrites (Batish et al., 2012) and that *MAP2*, *CaMKIIa* and *ACTB* RNAs localize independently in low copy numbers (Mikl et al., 2011), thus supporting the “sushi-belt model” (Doyle and Kiebler, 2011). The findings may also be corroborated by a rough estimate. Assuming that a HeLa cell contains about 200.000 transcripts in a volume of 3000 μm^3 there will be 60 mRNAs per μm^3 (Shapiro et al., 2013). By simple counting of SIM stacks, we observe 30-50 mRNPs per μm^3 , which is compatible with a single transcript in each mRNP, considering that some mRNAs may undergo translation or reside in the nucleus. RNA-binding proteins have been proposed to coordinate the production of functionally related proteins by organizing their mRNAs in regulons (Keene, 2007). The finding that small cytoplasmic mRNP granules represent singletons implies that coordinate expression of functionally related mRNAs in RNA regulons is unlikely to result from coordinated assembly, but rather results from regulated docking, as described above, or from selective stabilization of mRNA in the particles.

Small cytoplasmic mRNP granules are distinct from large stress granules and P bodies, that represent dynamic mRNP assemblies formed in response to stress and mRNA decay, respectively. Based on our findings, we

propose that smaller cytoplasmic granules should be designated mRNP singletons rather than granules to clearly distinguish them from the larger assemblies. Moreover, this would allude to the fact that stress granules probably incorporate elements of mRNP singletons.

Acknowledgements

The Danish National Program for Infrastructure is thanked for donating the super resolution microscope and Lena Bjørn Johansson is thanked for technical assistance.

Author Contributions

FCN and AM designed the study. AM, FCN, JC, FOB, CH designed the experiments. AM, FOB and JC performed the experiments. AM, FCN, JC, FOB and CH analysed the results. AM, FCN and JC prepared the manuscript. All authors read and approved the final manuscript.

Declaration of Interests

The authors declare no competing interests.

Methods

Contact for Reagent and Resource Sharing

Further information and requests for resources and reagents should be directed to and will be fulfilled by the Lead Contact, Finn Cilius Nielsen (finn.cilius.nielsen@regionh.dk).

Experimental model and Subject Details

Cell lines

HeLa cells (ATCC® CCL-2™) were cultured in phenol red-free Dulbecco's Modified Eagle Medium (DMEM), high glucose (4.5 g/L) + GlutaMAX and 1 mM sodium pyruvate (Thermo Fisher Scientific) supplemented with 10% Fetal bovine serum (Tetracycline free, Biowest) and penicillin/streptomycin (Invitrogen). HT1080 cells (ATCC® CCL-121™) were cultured in Dulbecco's Modified Eagle Medium (DMEM), high glucose (4.5 g/L) + GlutaMAX and 1 mM sodium pyruvate (Thermo Fisher Scientific) supplemented with 10% Fetal bovine serum (Tetracycline free, Biowest) and penicillin/streptomycin (Invitrogen). TREX HT1080 3xFLAG-IMP1 cells were cultured in Dulbecco's Modified Eagle Medium (DMEM), high glucose (4.5 g/L) + GlutaMAX and 1 mM sodium pyruvate (Thermo Fisher Scientific) supplemented with 10% Fetal bovine serum, 5 ug/mL Blastcidin (Thermo Fisher Scientific), 100 ug/ml Hygromycin (Thermo Fisher Scientific) and penicillin/streptomycin. All cell lines were grown at 37°C with 5% CO₂ in a humidified incubator

Method Details

Transfections

Vectors

IMP1 was cloned into pEGFP-C2 (Clontech) and pmEos3.2-C1 vector (Addgene). GFP-IMP1_KH1-4mut construct was obtained by mutating the GXXG loops of the 4 KH domains (Hollingworth et al., 2012) from GK(E/K/G)G to GELG. YBX1 was cloned into pcDNA3.1+N-EGFP (Genscript) and pmCherry-C1 (Clontech)

vectors, inserting a 25 amino acid flexible linker composed of 5x GlyGlyGlyGlySer between the fluorescent tag and YBX1 to reduce aggregation.

Plasmid transfections

HeLa cells were plated in 35mm glass-bottom dishes (P35G-1.5-14-C, MatTek) and were transfected using FuGENE® 6 (Promega). For each transfection, 3 µl of FuGENE® 6 and 1.3 µg of plasmid were added to 100 µl of OPTI-MEM Medium (Thermo Fisher Scientific) . The mixture was incubated at room temperature for 30 minutes prior to the addition to the coverslips.

siRNA and plasmid co-transfection

HeLa cells were plated in 35mm glass-bottom dishes (P35G-1.5-14-C, MatTek) and were transfected using Lipofectamine 2000 (Thermo Fisher Scientific). For each transfection, 3 µl of Lipofectamine® 2000, 1 µg of plasmid and siRNA to a final concentration of 2.5 nM were added to 100 µl of OPTI-MEM Medium (Thermo Fisher Scientific). The mixture was incubated at room temperature for 30 minutes prior to the addition to the coverslips.

Western blot analysis

Protein extracts were separated in 10% RunBlue SDS gels and transferred to PVDF membranes (Invitrogen). After blocking, membranes were incubated overnight with a peptide specific rabbit anti-IMP1 antibody (Nielsen et al., 1999) an anti-YBX1 antibody (ab12148, Abcam), an anti-GFP antibody (ab1218, Abcam) and a GAPDH antibody (FL-335, Santa Cruz) in blocking solution at 4°C before they were washed and incubated with horseradish peroxidase-conjugated anti-rabbit IgG for 1 h at room temperature. Immunoreactive proteins were detected with SuperSignal chemiluminescence reagents (Thermo Fisher Scientific) according to the manufacturer's instructions. Blots were scanned using a C-DiGit Blot Scanner (LI-COR Biosciences).

Immunoprecipitation

TREX HT1080 cells stably expressing 3xFLAG-IMP1 were generated as described (Jønson et al., 2007). Briefly, the expression of 3xFLAG-IMP1 was induced by the addition of 1 µg/ml tetracycline, and cells were harvested 24 hours after the addition of tetracycline in lysis buffer on ice. HT1080 cell line was used as a negative control. In parallel, HeLa cells were transiently transfected with pEGFP-C1 and pEGFP-IMP1 and cell pellets were collected 48 hours after transfection. Cell pellets containing 1×10^7 cells were lysed in lysis buffer containing 20 mM Tris-HCl (pH 7.5), 1.5 mM MgCl₂, 140 mM KCl, 1 mM DTT, 0.5% NP-40 supplemented with mammalian protease inhibitor cocktail (Sigma). Cell lysates were cleared by centrifugation at 8200 xg for 5 minutes before addition of EZview™ Red Anti-FLAG Affinity Gel (Sigma) or GFP antibody (ab1218, Abcam) coupled Dynabeads™ Protein G (Invitrogen). Cleared cell lysates were incubated with the beads for 2 hours at 4°C with rotation. After that, samples were washed 3x with lysis buffer, split and treated with 20 µg/mL RNase A (DNase and protease-free, Thermo Scientific) or RiboLock RNase inhibitor (Thermo Scientific) for 20 minutes at room temperature with rotation. Beads were subsequently washed and proteins were eluted directly in 2x SDS buffer.

Polysome fractionation analysis

Polysome analysis was performed as described (Nielsen et al., 2002). Briefly, HeLa cells (5×10^6 cells) were lysed in 500 µl 20 mM Tris-HCl (pH 8.5), 1.5 mM MgCl₂, 140 mM KCl, 0.5 mM DTT, 0.5% NP-40, 200 U of RNasin (Promega) per ml and 0.1 mM cycloheximide. The lysate was centrifuged at 10,000 xg for 10 min, and the supernatant was applied to a linear 20 to 47% sucrose gradient in 20 mM Tris-HCl (pH 8.0), 140 mM KCl, 5 mM MgCl₂. Centrifugation was carried out at 200,000 g for 2 hours and 15 min in a Beckman SW 41 rotor. Fractions of 1 ml were collected, followed by protein precipitation with 10% TCA.

Electrophoretic mobility-shift analysis (EMSA)

Electrophoretic mobility-shift analysis was carried out essentially as described previously (Nielsen et al., 2004). RNA targets were *C-MYC* CRD (positions 1181-1362 in CDS), *C-MYC* 3'UTR (positions 1-226 in 3'UTR), *ACTB* exon 5, and *ACTB* 3'UTR (positions 1-233). Tag-less recombinant human IMP1 and IMP1_KH1-4mut (with the four GXXG signature loops mutated to GELG) were expressed and purified as described earlier

(Nielsen et al., 2004). Recombinant human YBX1 with a C-terminal FLAG-tag was purchased from OriGene Technologies, Inc.

Immunofluorescence, fluorescence in situ hybridization and structured illumination microscopy (SIM).

HeLa cells were seeded in glass-bottom coverslips (P35G-0.170-14-C, MatTek) and fixed 24 hours after with 3.7% formaldehyde solution in PBS, followed by a permeabilization step with 0.5% Triton X-100 in PBS. Immunofluorescence of IMP1 and YBX1 was performed using antibodies against IMP-1 (E-20, Santa Cruz) and YBX1 (ab12148, Abcam). Nup153, eIF4A3 and eEF1a were detected using anti-Nup153 antibody (ab24700, Abcam), anti-eIF4A3 antibody (ab32485, Abcam) and anti-eEF1A1/2/L3 antibody (ab37969, Abcam). Coverslips were washed 3x with PBS prior to Alexa Fluor conjugated secondary antibodies (Thermo Fisher Scientific) incubation for an hour at RT. Samples were washed 3x with PBS and mounted in VECTASHIELD mounting media (RI = 1.45).

Structured Illumination Microscopy (SIM) was performed using a Zeiss ELYRA PS.1 microscope and channel correction was applied using a channel alignment file created by imaging 0.1 μ m TetraSpeck Microspheres (Thermo Fisher Scientific). The image sets comprised 5 rotations and processed images were thresholded in accordance with current standards to remove diffuse background (honeycombs) caused by stray pollutants or some residual autofluorescence on the SIM reconstructed pictures before contrasting. An example is provided in Supplemental Figure 6, that also provides a comparison between conventional confocal imaging and SIM of the mRNA granules and image overlays demonstrating the measurements of the granules.

RNA FISH of *ACTB* mRNA was performed with *ACTB* DesignReady Probe Set (LGC Biosearch Technologies) following the “Sequential Stellaris FISH and Immunofluorescence using Adherent Cells protocol” from LGC Biosearch Technologies

(https://biosearchassets.blob.core.windows.net/assets/bti_custom_stellaris_immunofluorescence_seq_protocol.pdf). Briefly, immunofluorescence of IMP1 and YBX1 was performed as described above followed by a fixation step with fixation buffer (3.7% formaldehyde in PBS), Wash Buffer A (LGC Biosearch Technologies)

was incubated for 5 minutes and *ACTB* probe set was hybridized in for 16 hours at 37°C with Hybridization buffer (LGC Biosearch Technologies). After hybridization, dishes were incubated with Wash Buffer A for 30 minutes at 37°C followed by addition and incubation of Wash Buffer B (LGC Biosearch Technologies) for 5 minutes. Samples were mounted and imaged using the same protocol described above.

OP-puromycin protein synthesis assay

HeLa cells were seeded in glass-bottom coverslips (Mattek) and Click-iT® Plus OPP Alexa Fluor® 488 Protein Synthesis Assay Kit was used to localize nascent polypeptides following the manufacturers protocol. Cycloheximide (50 µg/mL) was added prior to OPP to one sample as a negative control. After the click reaction, immunofluorescence detection of IMP1 and YBX1 was performed as described previously. Samples were mounted in Vectashield mounting medium and images were acquired using a Zeiss ELYRA 3.2 microscope (Structured Illumination Microscopy).

Photoconversion of mEos3.2-IMP1 for *in vivo* protein tracking

HeLa cells were plated in 35mm glass-bottom dishes (P35G-1.5-14-C, MatTek) and transfected with pmEos3.2-IMP1 with FuGENE 6 as described above in “Plasmid transfection” section. Photoconversion was performed using a Zeiss LSM780 microscope with a Plan-Apochromat 63x/1.4 Oil objective using a 405 laser pulse in a selected area in the cytoplasm. Cells were imaged before and after photoconversion and photoconverted mEos3.2-IMP1 was monitored every 10 seconds and followed throughout the cytoplasm.

Localization Microscopy

HeLa cells were stained with either IMP1 and YBX1 antibodies and Alexa Fluor 568 and Alexa Fluor 555 secondary antibodies, respectively, or with *ACTB* Quasar-570 probes (LGC Biosearch Technologies). Samples were mounted in non-hardening Vectashield mounting medium with a refraction index of 1.45 (Olivier et al., 2013). Localization Microscopy was performed on a Zeiss ELYRA PS.1 microscope using an alpha-Plan-Apochromat 100x/1.46 objective. Total internal reflection microscopy (TIRF) with a excitation wavelength of

561 nm and appropriate emission filters (BP 570-650) was used in all localization microscopy experiments and ZEN 2012 software was used to analyse and filter the data obtained in a total of 80.000 frames acquired. Frames were corrected for drift over a time scale of 36 min 13 sec (Model-based correction), and grouping was applied in the antibody stained samples in order to compile all the events that came from a single antibody. Frames corresponding to the bleaching period of the sample were discarded for the final counting.

Fluorescence correlation spectroscopy (FCS) and Fluorescence Cross Correlation Spectroscopy (FCCS)

FCS measurements were performed with a Zeiss LSM 780 confocal microscope. HeLa cells were transfected with pEGFP-C1 (GFP), GFP-IMP1, GFP-IMP1_KH1-4mut and GFP-YBX1 (-/+ cotransfection with YBX1 3'UTR siRNA) as described above in the *Plasmid transfection* and *siRNA and plasmid cotransfection* sections and incubated for ~16 h and 48 hours respectively before measurements were conducted. Argon laser with a 488 excitation wavelength was used making sure that the count rate was linear at each particular laser power used. Transfected cells were located and FCS measurements were performed in a Zeiss LSM780 confocal microscope using a C-Apochromat 40x/1.2 W Corr M27 objective. Measurements were recorded in 10 second intervals during a total time of 60 seconds choosing arbitrary points in the cytoplasm and experimental autocorrelation curves were obtained. Intervals showing bleaching were discarded for the average. GFP-IMP1 or GFP-IMP1_KH1-4mut and mCherry-YBX1 were cotransfected, and FCCS measurements were performed following the same procedure as with FCS.

CLIP-seq analysis

Five public datasets were acquired by use of fastq-dump (<https://trace.ncbi.nlm.nih.gov/Traces/sra/sra.cgi?view=software>) using the parameters: "skip-technical", "readids", "read-filter pass", "dumpbase", "split-files", and "clip". Fastq files were aligned with STAR (version 2.5.2b) (Dobin et al., 2013) to the GRCh38 release 87 genome assembly as provided by ENSEMBL with corresponding annotation (ftp://ftp.ensembl.org/pub/release-87/gtf/homo_sapiens/Homo_sapiens.GRCh38.87.gtf.gz), using an overhang of 50 for all samples. Aligned reads (bam files) were imported into GenomicAlignments (Lawrence et al., 2013) in R, and single end reads

were resized to the estimated fragment length (300bp) (Jothi et al., 2008). A standard peak calling algorithm could not be applied (e.g. MACS2) because of lack of a paired input sample. Hence, peaks were estimated from read pile-up (islands), where the lower boundary was estimated to be a cutoff where the mock samples proximate one island per transcript (closest number). In one case a mock was not available with the sample, and the lower boundary was estimated from median of mocks from ENCODE. All mock samples analysed required a cut-off lower than 9 reads in order to proximate one island per transcript. Crosslinked immunoprecipitation of endogenous YBX1 followed by high-throughput sequencing (CLIP-seq) in human MDA-parental breast cancer cells, YBX1 were acquired from the short read archive (SRA) with accession numbers: SRR1662159, SRR1662160, and SRR1662161 (Goodarzi et al., 2015). Enhanced CLIP-seq for IGF2BP1/IMP1 was acquired from SRA, accession numbers: SRR5112331 and SRR5112330 (Consortium, 2012).

References

- Anderson, P., and Kedersha, N. (2006). RNA granules. *J Cell Biol* 172, 803-808.
- Batish, M., van den Bogaard, P., Kramer, F.R., and Tyagi, S. (2012). Neuronal mRNAs travel singly into dendrites. *Proc Natl Acad Sci U S A* 109, 4645-4650.
- Bell, J.L., Wachter, K., Muhleck, B., Pazaitis, N., Kohn, M., Lederer, M., and Huttelmaier, S. (2013). Insulin-like growth factor 2 mRNA-binding proteins (IGF2BPs): post-transcriptional drivers of cancer progression? *Cell Mol Life Sci* 70, 2657-2675.
- Bommert, K.S., Effenberger, M., Leich, E., Kuspert, M., Murphy, D., Langer, C., Moll, R., Janz, S., Mottok, A., Weissbach, S., *et al.* (2013). The feed-forward loop between YB-1 and MYC is essential for multiple myeloma cell survival. *Leukemia* 27, 441-450.
- Buxbaum, A.R., Wu, B., and Singer, R.H. (2014). Single beta-actin mRNA detection in neurons reveals a mechanism for regulating its translatability. *Science* 343, 419-422.
- Consortium, E.P. (2012). An integrated encyclopedia of DNA elements in the human genome. *Nature* 489, 57-74.
- Conway, A.E., Van Nostrand, E.L., Pratt, G.A., Aigner, S., Wilbert, M.L., Sundararaman, B., Freese, P., Lambert, N.J., Sathe, S., Liang, T.Y., *et al.* (2016). Enhanced CLIP Uncovers IMP Protein-RNA Targets in Human Pluripotent Stem Cells Important for Cell Adhesion and Survival. *Cell Rep* 15, 666-679.
- Courchaine, E.M., Lu, A., and Neugebauer, K.M. (2016). Droplet organelles? *EMBO J* 35, 1603-1612.
- Darnell, J.C., and Richter, J.D. (2012). Cytoplasmic RNA-binding proteins and the control of complex brain function. *Cold Spring Harb Perspect Biol* 4, a012344.
- Dobin, A., Davis, C.A., Schlesinger, F., Drenkow, J., Zaleski, C., Jha, S., Batut, P., Chaisson, M., and Gingeras, T.R. (2013). STAR: ultrafast universal RNA-seq aligner. *Bioinformatics* 29, 15-21.
- Doyle, M., and Kiebler, M.A. (2011). Mechanisms of dendritic mRNA transport and its role in synaptic tagging. *EMBO J* 30, 3540-3552.
- Eliscovich, C., Shenoy, S.M., and Singer, R.H. (2017). Imaging mRNA and protein interactions within neurons. *Proc Natl Acad Sci U S A* 114, E1875-E1884.
- Evdokimova, V., Ovchinnikov, L.P., and Sorensen, P.H. (2006). Y-box binding protein 1: providing a new angle on translational regulation. *Cell Cycle* 5, 1143-1147.
- Evdokimova, V., Ruzanov, P., Imataka, H., Raught, B., Svitkin, Y., Ovchinnikov, L.P., and Sonenberg, N. (2001). The major mRNA-associated protein YB-1 is a potent 5' cap-dependent mRNA stabilizer. *EMBO J* 20, 5491-5502.

- Gerstberger, S., Hafner, M., and Tuschl, T. (2014). A census of human RNA-binding proteins. *Nat Rev Genet* 15, 829-845.
- Goodarzi, H., Liu, X., Nguyen, H.C., Zhang, S., Fish, L., and Tavazoie, S.F. (2015). Endogenous tRNA-Derived Fragments Suppress Breast Cancer Progression via YBX1 Displacement. *Cell* 161, 790-802.
- Hafner, M., Landthaler, M., Burger, L., Khorshid, M., Hausser, J., Berninger, P., Rothballer, A., Ascano, M., Jr., Jungkamp, A.C., Munschauer, M., et al. (2010). Transcriptome-wide identification of RNA-binding protein and microRNA target sites by PAR-CLIP. *Cell* 141, 129-141.
- Hansen, T.V.O., Hammer, N.A., Nielsen, J., Madsen, M., Dalbaeck, C., Wewer, U.M., Christiansen, J., and Nielsen, F.C. (2004). Dwarfism and Impaired Gut Development in Insulin-Like Growth Factor II mRNA-Binding Protein 1-Deficient Mice. *Molecular and Cellular Biology* 24, 4448-4464.
- Hoelz, A., Debler, E.W., and Blobel, G. (2011). The structure of the nuclear pore complex. *Annu Rev Biochem* 80, 613-643.
- Hollingworth, D., Candel, A.M., Nicastro, G., Martin, S.R., Briata, P., Gherzi, R., and Ramos, A. (2012). KH domains with impaired nucleic acid binding as a tool for functional analysis. *Nucleic Acids Res* 40, 6873-6886.
- Jonson, L., Christiansen, J., Hansen, T.V., Vikesa, J., Yamamoto, Y., and Nielsen, F.C. (2014). IMP3 RNP safe houses prevent miRNA-directed HMGA2 mRNA decay in cancer and development. *Cell Rep* 7, 539-551.
- Jothi, R., Cuddapah, S., Barski, A., Cui, K., and Zhao, K. (2008). Genome-wide identification of in vivo protein-DNA binding sites from ChIP-Seq data. *Nucleic Acids Res* 36, 5221-5231.
- Jønson, L., Vikesaa, J., Krogh, A., Nielsen, L.K., Hansen, T.v., Borup, R., Johnsen, A.H., Christiansen, J., and Nielsen, F.C. (2007). Molecular composition of IMP1 ribonucleoprotein granules. *MCP* 6, 798-811.
- Keene, J.D. (2007). RNA regulons: coordination of post-transcriptional events. *Nat Rev Genet* 8, 533-543.
- Kiebler, M.A., and Bassell, G.J. (2006). Neuronal RNA granules: movers and makers. *Neuron* 51, 685-690.
- Knockenbauer, K.E., and Schwartz, T.U. (2016). The Nuclear Pore Complex as a Flexible and Dynamic Gate. *Cell* 164, 1162-1171.
- Krichevsky, A.M., and Kosik, K.S. (2001). Neuronal RNA granules: a link between RNA localization and stimulation-dependent translation. *Neuron* 32, 683-696.
- Kumari, P., Gilligan, P.C., Lim, S., Tran, L.D., Winkler, S., Philp, R., and Sampath, K. (2013). An essential role for maternal control of Nodal signaling. *Elife* 2, e00683.

- Lawrence, M., Huber, W., Pages, H., Aboyoun, P., Carlson, M., Gentleman, R., Morgan, M.T., and Carey, V.J. (2013). Software for computing and annotating genomic ranges. *PLoS Comput Biol* **9**, e1003118.
- Leeds, P., Kren, B.T., Boylan, J.M., Betz, N.A., Steer, C.J., Gruppuso, P.A., and Ross, J. (1997). Developmental regulation of CRD-BP, an RNA-binding protein that stabilizes c-myc mRNA in vitro. *Oncogene* **14**, 1279-1286.
- Liu, J., Xu, Y., Stoleru, D., and Salic, A. (2012). Imaging protein synthesis in cells and tissues with an alkyne analog of puromycin. *Proc Natl Acad Sci U S A* **109**, 413-418.
- Lu, W., Winding, M., Lakonishok, M., Wildonger, J., and Gelfand, V.I. (2016). Microtubule-microtubule sliding by kinesin-1 is essential for normal cytoplasmic streaming in *Drosophila* oocytes. *Proc Natl Acad Sci U S A* **113**, E4995-5004.
- Maquat, L.E., Tarn, W.Y., and Isken, O. (2010). The pioneer round of translation: features and functions. *Cell* **142**, 368-374.
- Mateyak, M.K., and Kinzy, T.G. (2010). eEF1A: thinking outside the ribosome. *J Biol Chem* **285**, 21209-21213.
- Mikl, M., Vendra, G., and Kiebler, M.A. (2011). Independent localization of MAP2, CaMKIIalpha and beta-actin RNAs in low copy numbers. *EMBO Rep* **12**, 1077-1084.
- Milo, R., Jorgensen, P., Moran, U., Weber, G., and Springer, M. (2010). BioNumbers--the database of key numbers in molecular and cell biology. *Nucleic Acids Res* **38**, D750-753.
- Molliex, A., Temirov, J., Lee, J., Coughlin, M., Kanagaraj, A.P., Kim, H.J., Mittag, T., and Taylor, J.P. (2015). Phase separation by low complexity domains promotes stress granule assembly and drives pathological fibrillization. *Cell* **163**, 123-133.
- Nielsen, F.C., Nielsen, J., and Christiansen, J. (2001). A family of IGF-II mRNA binding proteins (IMP) involved in RNA trafficking. *Scand J Clin Lab Invest Suppl* **234**, 93-99.
- Nielsen, F.C., Nielsen, J., Kristensen, M., Koch, G., and Christiansen, J. (2002). Cytoplasmic trafficking of IGF-II mRNA-binding protein by conserved KH domains. *J Cell Sci* **115**, 2087-2097.
- Nielsen, J., Adolph, S., Rajpert-De Meyts, E., Lykke-Andersen, J., Koch, G., Christiansen, J., and Nielsen, F. (2003). Nuclear transit of human zipcode-binding protein IMP1. *The Biochemical journal* **376**, 383-391.
- Nielsen, J., Christiansen, J., Lykke-Andersen, J., Johnsen, A.H., Wewer, U.M., and Nielsen, F.C. (1999). A family of insulin-like growth factor II mRNA-binding proteins represses translation in late development. *Mol Cell Biol* **19**, 1262-1270.

- Nielsen, J., Kristensen, M.A., Willemoes, M., Nielsen, F.C., and Christiansen, J. (2004). Sequential dimerization of human zipcode-binding protein IMP1 on RNA: a cooperative mechanism providing RNP stability. *Nucleic Acids Res* 32, 4368-4376.
- Nishino, J., Kim, S., Zhu, Y., Zhu, H., and Morrison, S.J. (2013). A network of heterochronic genes including Imp1 regulates temporal changes in stem cell properties. *Elife* 2, e00924.
- Oleynikov, Y., and Singer, R.H. (2003). Real-time visualization of ZBP1 association with beta-actin mRNA during transcription and localization. *Curr Biol* 13, 199-207.
- Olivier, N., Keller, D., Rajan, V.S., Gonczy, P., and Manley, S. (2013). Simple buffers for 3D STORM microscopy. *Biomed Opt Express* 4, 885-899.
- Reijns, M.A., Alexander, R.D., Spiller, M.P., and Beggs, J.D. (2008). A role for Q/N-rich aggregation-prone regions in P-body localization. *J Cell Sci* 121, 2463-2472.
- Ross, A.F., Oleynikov, Y., Kislauskis, E.H., Taneja, K.L., and Singer, R.H. (1997). Characterization of a beta-actin mRNA zipcode-binding protein. *Mol Cell Biol* 17, 2158-2165.
- Runge, S., Nielsen, F.C., Nielsen, J., Lykke-Andersen, J., Wewer, U.M., and Christiansen, J. (2000). H19 RNA binds four molecules of insulin-like growth factor II mRNA-binding protein. *J Biol Chem* 275, 29562-29569.
- Shapiro, E., Biezuner, T., and Linnarsson, S. (2013). Single-cell sequencing-based technologies will revolutionize whole-organism science. *Nat Rev Genet* 14, 618-630.
- Shiota, M., Izumi, H., Onitsuka, T., Miyamoto, N., Kashiwagi, E., Kidani, A., Yokomizo, A., Naito, S., and Kohno, K. (2008). Twist promotes tumor cell growth through YB-1 expression. *Cancer Res* 68, 98-105.
- Shyu, A.B., and Wilkinson, M.F. (2000). The double lives of shuttling mRNA binding proteins. *Cell* 102, 135-138.
- Singh, G., Pratt, G., Yeo, G.W., and Moore, M.J. (2015). The Clothes Make the mRNA: Past and Present Trends in mRNP Fashion. *Annu Rev Biochem* 84, 325-354.
- Skabkin, M.A., Kiselyova, O.I., Chernov, K.G., Sorokin, A.V., Dubrovin, E.V., Yaminsky, I.V., Vasiliev, V.D., and Ovchinnikov, L.P. (2004). Structural organization of mRNA complexes with major core mRNP protein YB-1. *Nucleic Acids Res* 32, 5621-5635.
- Song, T., Zheng, Y., Wang, Y., Katz, Z., Liu, X., Chen, S., Singer, R.H., and Gu, W. (2015). Specific interaction of KIF11 with ZBP1 regulates the transport of beta-actin mRNA and cell motility. *J Cell Sci* 128, 1001-1010.
- Stelzer, E.H. (2014). Better imaging through chemistry. *Cell* 159, 1243-1246.

- Suzuki, K., Miyazaki, M., Takagi, J., Itabashi, T., and Ishiwata, S. (2017). Spatial confinement of active microtubule networks induces large-scale rotational cytoplasmic flow. *Proc Natl Acad Sci U S A* **114**, 2922-2927.
- Uchiumi, T., Fotovati, A., Sasaguri, T., Shibahara, K., Shimada, T., Fukuda, T., Nakamura, T., Izumi, H., Tsuzuki, T., Kuwano, M., *et al.* (2006). YB-1 is important for an early stage embryonic development: neural tube formation and cell proliferation. *J Biol Chem* **281**, 40440-40449.
- Wu, B., Buxbaum, A.R., Katz, Z.B., Yoon, Y.J., and Singer, R.H. (2015). Quantifying Protein-mRNA Interactions in Single Live Cells. *Cell* **162**, 211-220.
- Yaniv, K., and Yisraeli, J.K. (2002). The involvement of a conserved family of RNA binding proteins in embryonic development and carcinogenesis. *Gene* **287**, 49-54.
- Zhang, M., Chang, H., Zhang, Y., Yu, J., Wu, L., Ji, W., Chen, J., Liu, B., Lu, J., Liu, Y., *et al.* (2012). Rational design of true monomeric and bright photoactivatable fluorescent proteins. *Nat Methods* **9**, 727-729.

Graphical abstract

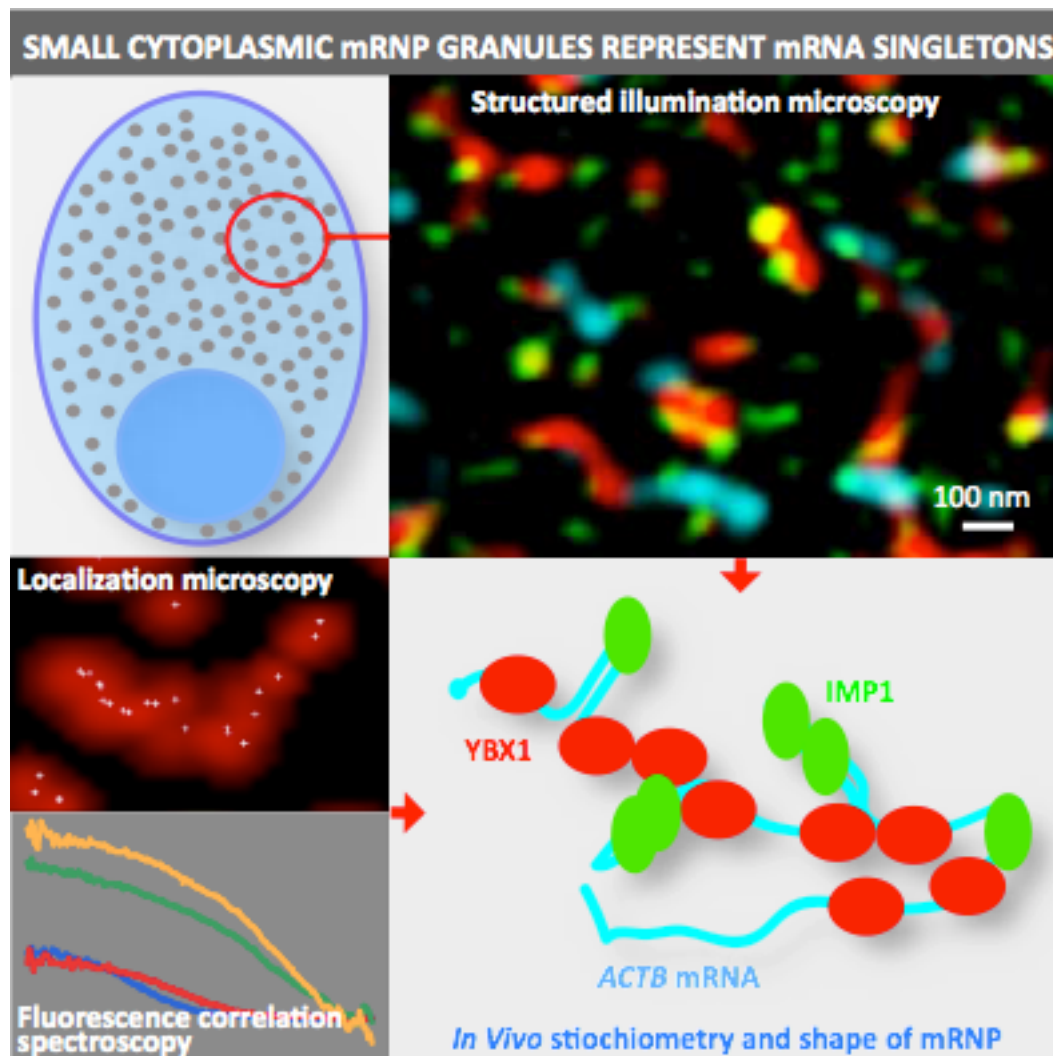




Figure 1. Schematic representation of YBX1 and IMP1 RNA-binding proteins.

YBX1 is composed of a cold-shock domain (CSD) depicted in blue and a number of predicted low-complexity sequences (LCS) shown in yellow. IMP1 is composed of two RNA recognition modules (RRM) and four K homology domains (KH), the latter being responsible for IMP1 mRNA binding. Moreover, a short low-complexity sequence is predicted between domains KH2 and KH3.

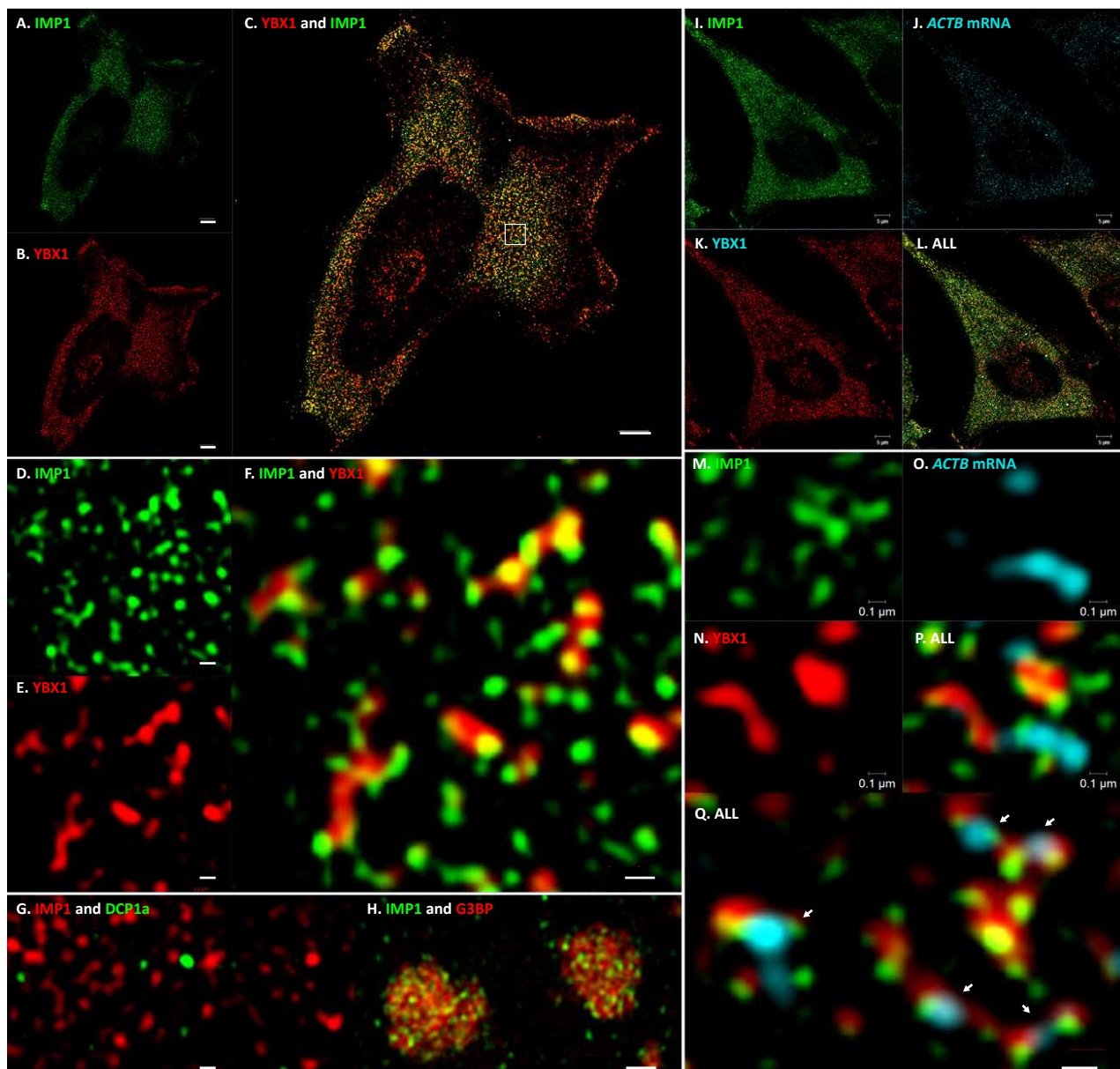


Figure 2. Structure of IMP1 and YBX1 and *ACTB* mRNA mRNP granules.

A-F, HeLa cells were stained with anti-IMP1 and anti-YBX1 antibodies followed by Alexa fluor 488 (green) and Alexa fluor 647 (red) secondary antibodies, respectively. **A-C**, an overview of the cell and **D-F**, a blow up of IMP1 and YBX1 granules in the indicated area (white square) in panel **C**. **G**, P bodies depicted by DCP1a-EGFP in combination with IMP1 staining and **H**, pHcRed-G3BP in stress granules in combination with IMP1 staining. Note that IMP1 is labelled with Alexa fluor 647 (red) in panel **G**. **I-L**, IMP1 (**I**), YBX1 (**J**) and *ACTB* mRNA FISH (**K**) employing 48 Quasar-570 (cyan) labelled oligonucleotides corresponding to the entire *ACTB* mRNA combined with IMP1 (Alexa Fluor 488, green) and YBX1 (Alexa Fluor 660, red) (**L**). **M-Q**, blow up of *ACTB* mRNA and IMP1-YBX1 containing granules. Scale bars: A-C 5 μ m; D-F 0.2 μ m; G and H 0.2 μ m; I-L 5 μ m; M-Q 0.1 μ m.

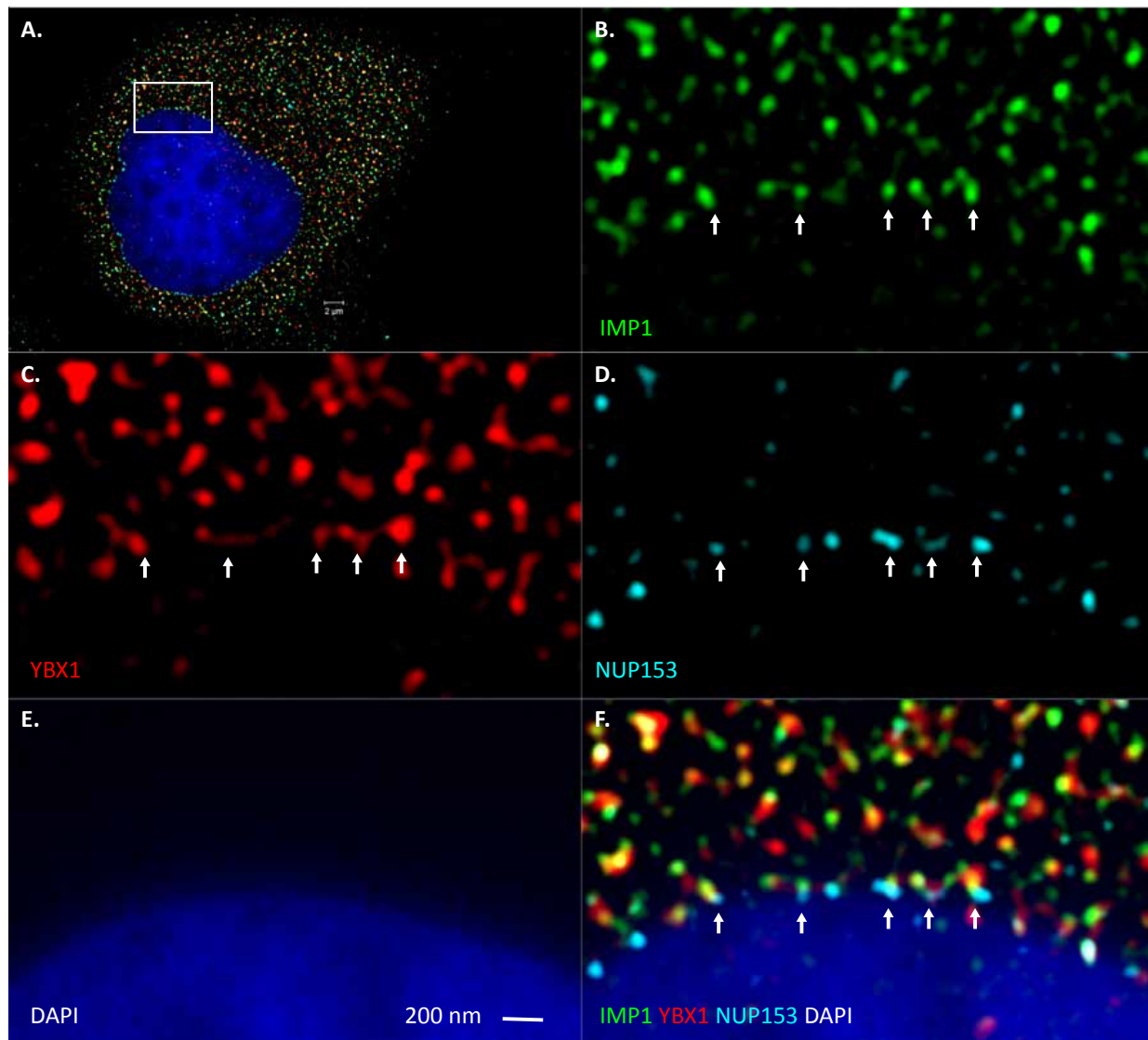


Figure 3. IMP1 and YBX1 mRNP formation at the nuclear pore.

Hela cells were stained with anti-IMP1, anti-YBX1 and anti-NUP153 primary antibodies followed by Alexa fluor 488 (green), Alexa 555 (cyan) and Alexa fluor 647 (red) secondary antibodies, respectively. Moreover, the nucleus was stained with DAPI (deep blue). **A**, Overview of a triple-stained cell and the area that is shown in the blow up below. **B-E**, Individual IMP1, YBX1, Nup153 and DAPI stainings. **F**, Composite picture demonstrating the colocalization of Nup153 and the IMP1_YBX1 mRNP. Arrows indicate nuclear pores.

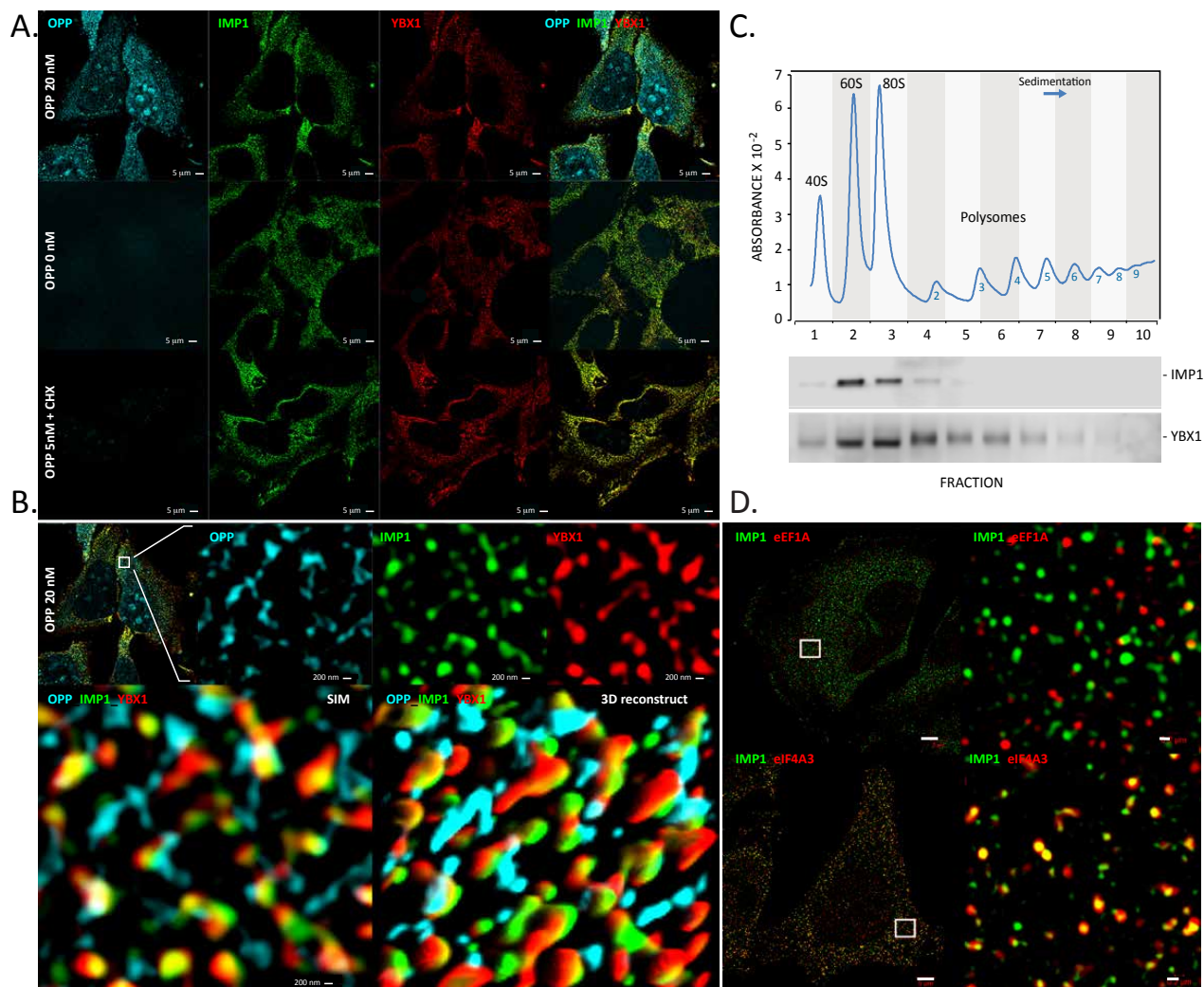


Figure 4. IMP1 and YBX1 mRNP granules do not associate with the translational apparatus. Translating ribosomes were labelled with O-propargyl puromycin (OPP) followed by puromycin-based click conjugation of Alexa Fluor 488 (cyan). IMP1 and YBX1 were stained with anti-IMP1 and anti-YBX1 antibodies followed by Alexa Fluor 568 (green) and Alexa Fluor 647 (red) secondary antibodies, respectively. **A**, Ribosome, IMP1 and YBX1 stainings with and without addition of 20 nM OPP and in the presence of cycloheximide (CHX). **B**, Blowup of the individual mRNP and 3D reconstruction of 10 consecutive slices demonstrating the vicinity of ribosomes and mRNP. **C**, Polysome fractionation analysis and subsequent immunodetection of IMP1 and YBX1 by Western Blot. The upper panel depicts the A260 sedimentation profile, whereas the lower panel shows the corresponding Western analysis of the fractions. The sedimentation of 80S monosomes and ribosomal subunits is indicated, and the polysomes are numbered according to the number of loaded 80S complexes. **D**, IMP1 immunofluorescence stainings in combination with eEF1A or eIF4A3.

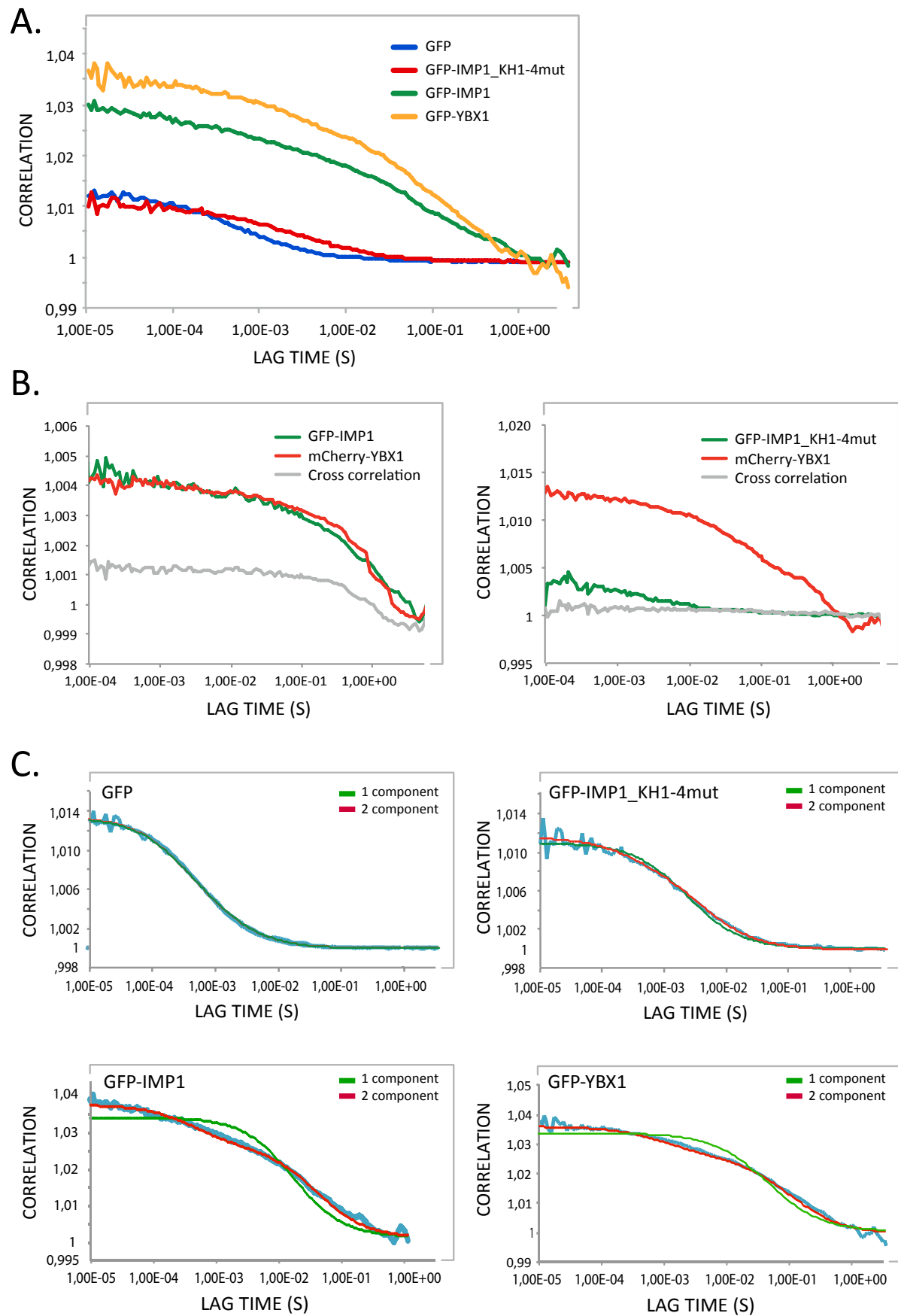
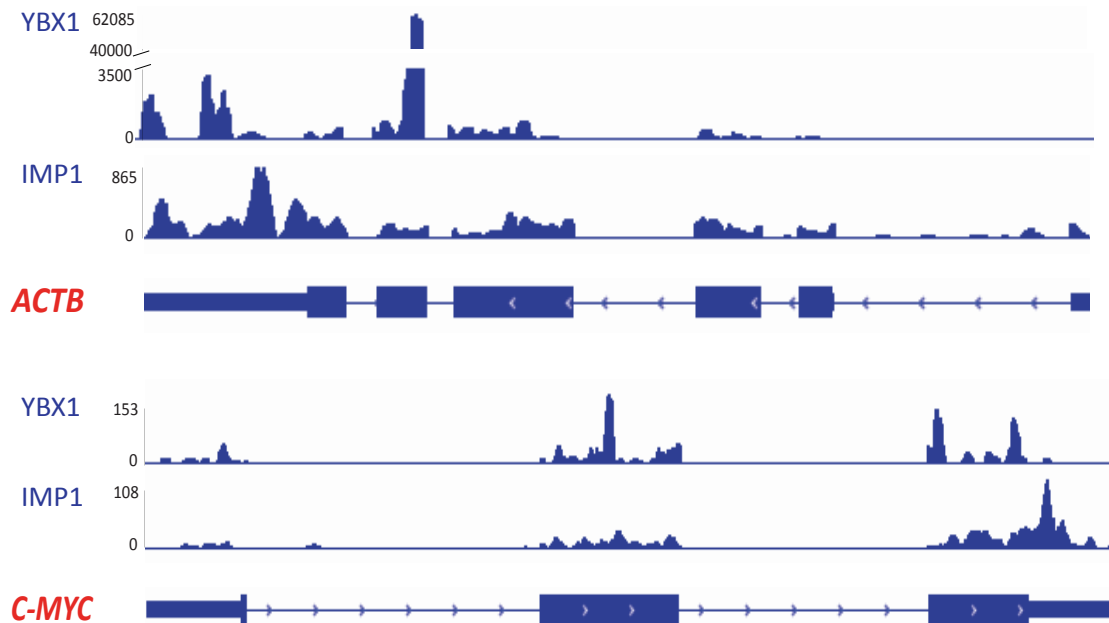


Figure 5. IMP1_YBX1 mRNP dynamics.

GFP- and mCherry-tagged IMP1, YBX1 and IMP1 mutated in the four GXXG loops (GFP-IMP1_KH1-4mut) were expressed in HeLa cells, and their dynamic behaviour was recorded by Fluorescence Correlation Spectroscopy (FCS). **A**, Autocorrelation curves of cytoplasmic GFP, GFP-IMP1, GFP-YBX1 and GFP-IMP1_KH1-4mut. **B**, Cross-Correlation curves of cells co-transfected with GFP-IMP1 and mCherry-YBX1 or co-transfected with GFP-IMP1_KH1-4mut and mCherry-YBX1. **C**, Autocorrelation curves of the different constructs shown in panel A together with the fittings to 1- and 2- component diffusion models.

A.



B.

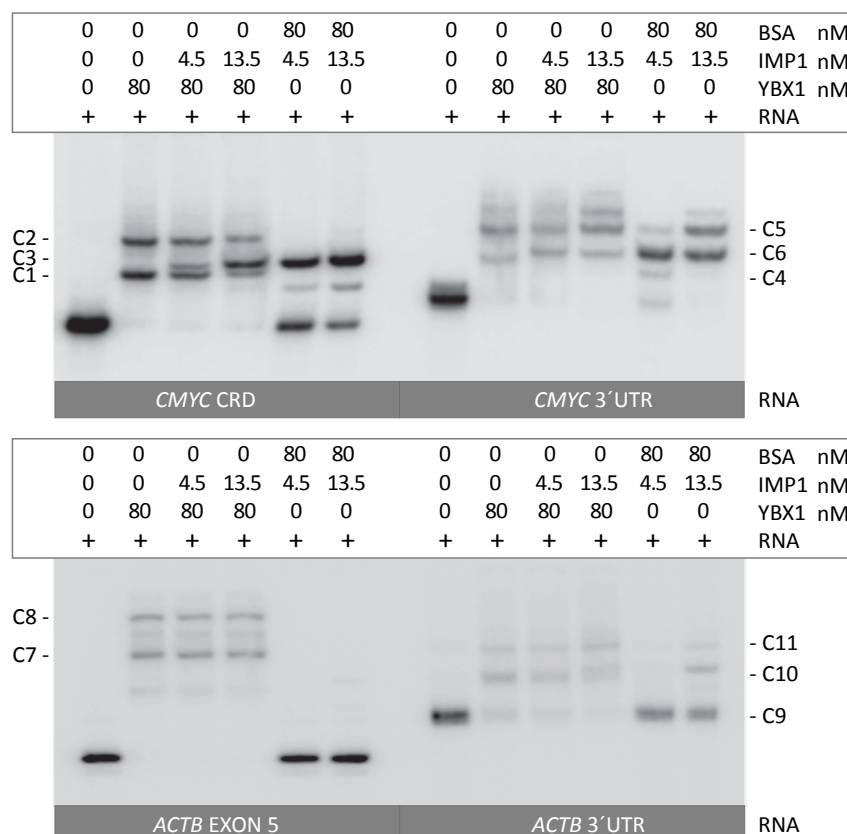


Figure 6. RNA-binding properties of IMP1 and YBX1.

A, YBX1 RIP-seq and IMP1 eCLIP data from *ACTB* and *C-MYC* mRNAs. **B**, Electrophoretic mobility-shift assay (EMSA) of single or combinations of IMP1 and YBX1 proteins with 32 P-labelled *C-MYC* coding region determinant (CRD), *C-MYC* 3'UTR, *ACTB* Exon5, or *ACTB* 3'UTR.

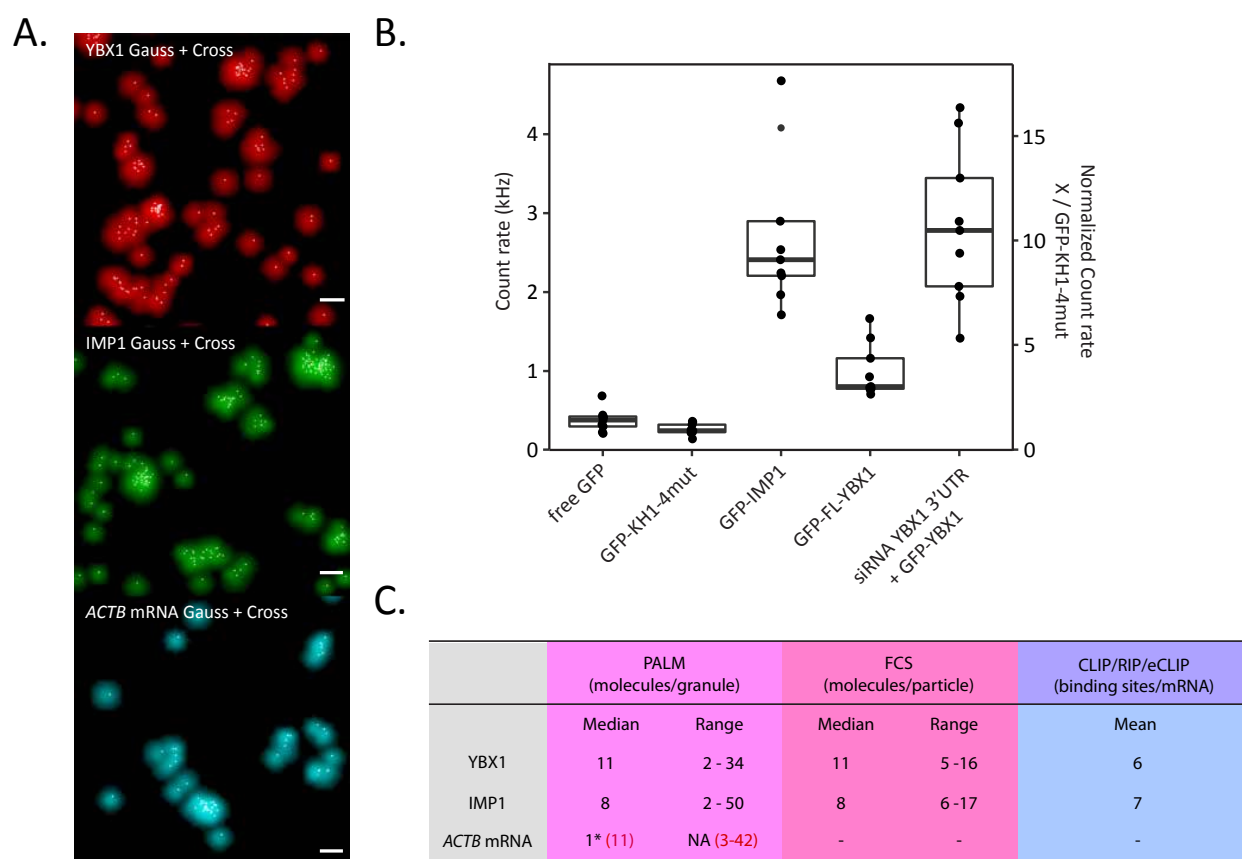


Figure 7. Molecular composition of IMP1_YBX1 mRNP.

The number of IMP1, YBX1 and *ACTB* mRNA molecules in the mRNP were derived from Localization Microscopy (LM) or from FCS and compared to the average number of binding sites in the transcriptome from eCLIP and RIP-seq analysis. For Localization Microscopy cells were stained for IMP1, YBX1 and *ACTB* mRNA, and following bleaching mRNP emitted photons were counted as described. **A**, Examples of the Localization Microscopy images of YBX1 (red), IMP1 (green) and *ACTB* mRNA (cyan), respectively. Scale Bar 100 nm **B**, Counts per particle derived from Fluorescence Correlation Spectroscopy of cells transfected with GFP, GFP-IMP1_KH1-4mut, GFP-IMP1, GFP-YBX1, and with co-transfection of YBX1 3'UTR-directed siRNA and GFP-YBX1. Laser power was 0.02% in all measurements. **C**, Summary of the data from Localization Microscopy, FCS, and binding sites predicted from either eCLIP (IMP1) or RIP-seq (YBX1) experiments.